GT2015-42773

DNS OF FLOW IN A LOW-PRESSURE TURBINE CASCADE USING A DISCONTINUOUS-GALERKIN SPECTRAL-ELEMENT METHOD

Anirban Garai
Oak Ridge Associated Universities
NASA Ames Research Center
Moffett Field, CA, USA

Laslo Diosady
Science and Technology Corporation
NASA Ames Research Center
Moffett Field, CA, USA

Scott Murman
NASA Ames Research Center
Moffett Field, CA, USA

Nateri Madavan
NASA Ames Research Center
Moffett Field, CA, USA

ABSTRACT

A new computational capability under development for accurate and efficient high-fidelity direct numerical simulation (DNS) and large eddy simulation (LES) of turbomachinery is described. This capability is based on an entropy-stable Discontinuous-Galerkin spectral-element approach that extends to arbitrarily high orders of spatial and temporal accuracy and is implemented in a computationally efficient manner on a modern high performance computer architecture. A validation study using this method to perform DNS of flow in a low-pressure turbine airfoil cascade is presented. The results indicate that the method captures the main features of the flow.

NOMENCLATURE

C	Axial chord length
E	Total energy
$\boldsymbol{F}$	Flux vector
H	Enthalpy
Ma	Mach number
$\boldsymbol{Q}$	Entropy variable
Re	Reynolds number
T	Temperature
U	Speed
a	Speed of sound
$\boldsymbol{n}$	Normal direction
p	Pressure
$\boldsymbol{q}$	Conservative variable
s	Entropy
t	Time
$\boldsymbol{v}$	Velocity vector
w	Basis function

x	Coordinate direction
y	Coordinate direction
z	Coordinate direction
β	Flow angle
γ	Specific gas constant
δ	Boundary-layer thickness
η	Wall-normal direction
κ	Thermal conductivity
λ	Bulk viscosity
μ	Viscosity
ξ	Tangential direction
ρ	Density
τ_w	Viscous stress

Superscripts

I	Inviscid
V	Viscous

Subscripts

1	Inlet
2	Exit
is	Isentropic
n	Surface normal
t	Total properties

INTRODUCTION

The numerical simulation of turbomachinery flows is a challenging problem for Computational Fluid Dynamics. These flows involve both complex physics, such as wake impingement upon blades, and acoustics, and complex moving geometries to resolve the tight clearances between components, especially near the tip region.

Over the past several decades, turbomachinery flow simulation capability has advanced from the early one-dimensional, steady, inviscid and viscous approximations to steady and unsteady two- and three-dimensional approaches capable of solving the Reynolds-Averaged Navier-Stokes equation (RANS) in multistage settings. The current RANS-based methods have proven extremely useful, although their inherent limitations in modeling transitional and turbulent flows in complex configurations are well recognized. In recent years, the rapid expansion of high performance computing capability has led to attention being focused on high fidelity simulation techniques, such as DNS and LES. These techniques offer the promise of more accurate and better resolved simulations that can shed more light on the complicated flow phenomena and lead to improved turbomachinery designs.

There are several studies reported in the recent literature on applying DNS and LES techniques to turbomachinery applications. Using incompressible DNS methods, Wu and Durbin [1], Wissink and coworkers (see, for example, [2], [3]) studied flow transition in turbine cascades due to freestream turbulence and incoming wakes, and Zaki et al. [5] studied the effect of freestream turbulence in a compressor cascade. Rai applied compressible DNS techniques in conjunction with overset-grid techniques to simulate transitional flow in a turbine stator passage [6]; these techniques were later extended to turbine and compressor stage configurations [7-9] where the effects of rotor-stator interaction were studied. More recently, Sandberg et al. [10, 11] and Michelassi et al. [12] have reported efficient DNS simulations of a low-pressure turbine cascade. All these simulations were performed on idealized mid-span configurations and at low Reynolds number in order to keep computational resources reasonable. Note that these references are merely a sampling and by no means represent the entire body of prior work that has been reported in this area. In addition to DNS studies, several researchers have focused on the application of LES methods. Michelassi et al. [13] performed LES of turbine cascades at conditions that match reference DNS data. The influence of freestream turbulence on transition in turbine and compressor blading has been investigated using LES by Raverdy et al. [14], Matsuura and Kato [15], Sarkar and Voke [16], Medic and Sharma [17], and others. In addition to these efforts, DNS and LES techniques have also been successfully used to study other turbomachinery flow features, such as tip clearance flows [18], noise generation due to entropy waves [19], and blade cooling effects.

Many of the studies in the literature have made use of high-order spatial finite-difference and finite-volume techniques because of their superiority in resolving a wide range of spatial and temporal scales using coarser meshes compared to traditional second-order methods. For example, Sandberg et al. [10, 11] and Michelassi et al. [12] used fourth-order compact finite difference schemes to study the effect of freestream turbulence on the transitional flow in a turbine cascade, while Rai [6-9] made use of high-order upwind-biased schemes.

There is growing interest in the development and use of Discontinuous-Galerkin (DG) methods due to their attractive features for high-accuracy numerical simulations of a variety of fluid flow configurations. In addition to the ability to formulate arbitrarily high-order schemes while maintaining a compact numerical stencil, DG methods are extremely flexible and can handle a variety of element types and mesh topologies. They are thus computationally efficient, and also allow a number of adaptation techniques and solver acceleration strategies to be implemented in a straightforward manner. For these reasons, these methods have become the focus of recent research. In the past few years, these methods are being evaluated for turbomachinery applications. Work on RANS-based turbomachinery simulations using DG methods was first reported by Bassi et al. [20] and, more recently, in Refs. [21-23]. DNS simulations of turbomachinery configurations using these methods have recently been reported by de Wiart et al. [24] and Hillewaert et al. [25]. The results presented in this paper represent research work in this direction.

This paper describes a new computational capability for accurate and efficient high-fidelity direct numerical simulations (DNS) and large eddy simulations (LES) for turbomachinery applications. This capability is based on an entropy-stable Discontinuous Galerkin spectral-element approach for compressible flows that extends to arbitrarily high orders of spatial and temporal accuracy and is implemented in a computationally efficient manner on a modern high performance computer architecture. This capability will advance turbomachinery flow simulation beyond the current reliance on steady and unsteady RANS methods with their inherent limitations. It will serve as a valuable analysis tool to understand complicated flow phenomena, such as rotor-stator interaction and tip clearance effects, and will ultimately help lead to improved turbomachinery designs where their detrimental effects on performance and operability are mitigated.

As a first step towards developing a general capability, the DNS of transitional and turbulent flow in a turbine cascade using an entropy-stable DG spectral-element method is presented in this paper. The method has previously been validated using simulations of Taylor-Green vortex evolution, compressible channel flow, and the flow over periodic hills [26, 27]. A variational multiscale method (a reformulation of the classical LES formulation) is implemented [28] that also allows the simulation of high-Reynolds number compressible flows where DNS is impractical and RANS-based approaches are inadequate. Here, the method is extended for turbomachinery applications, and validation results are presented for flow in a turbine-stator passage. The flow configuration is the T106A-EIZ low-pressure turbine (LPT) cascade [29] that has been the subject of many experimental and computational studies. The main objective of this paper is to validate the present methodology and demonstrate its future potential in predicting challenging turbomachinery flow phenomena and addressing the needs of the turbulence modeling community in their efforts to improve RANS-based capabilities.

NUMERICAL METHOD

The compressible Navier-Stokes equations are solved for an ideal gas with constant specific heat coefficients in an entropy stable formulation. The governing equations in conservative form can be written as:

$$\boldsymbol{q}_{,t} + (\boldsymbol{F}_i^I + \boldsymbol{F}_i^V)_i = 0, \tag{1}$$

where, $\boldsymbol{q} = [\rho,\ \rho\boldsymbol{v}, \rho E]$ is the conservative state vector, $\boldsymbol{F}^I = [\rho\boldsymbol{v},\ \rho\boldsymbol{v}\boldsymbol{v}^T + p\boldsymbol{I},\ \rho\boldsymbol{v}H]$ is the inviscid flux vector and $\boldsymbol{F}^V = [0,\ \boldsymbol{\tau},\ \boldsymbol{\tau}\boldsymbol{v} - \kappa_T \nabla T]$ is the viscous flux, with $\boldsymbol{\tau} = \mu(\nabla\boldsymbol{v} + \nabla\boldsymbol{v}^T) - \mu\lambda(\nabla\cdot\boldsymbol{v})I$.

Transforming from conservative to entropy variables, $\boldsymbol{q} = \boldsymbol{q}(\boldsymbol{Q})$, Eqn. (1) takes the form:

$$A_0 \boldsymbol{Q}_{,t} + A_i \boldsymbol{Q}_{,i} - \left(K_{ij}\boldsymbol{Q}_{,x_j}\right)_{,i} = 0, \tag{2}$$

with symmetric $A_0 = \boldsymbol{q}_{\boldsymbol{Q}}$, $A_i = \boldsymbol{F}_{i,\boldsymbol{q}}^I A_0$, and $K_{ij} = \boldsymbol{F}_{i,\boldsymbol{q}_{,x_j}}^V A_0$; Here, the entropy variables are given as:

$$\boldsymbol{Q} = \left[-\frac{s}{\gamma-1} + \frac{\gamma+1}{\gamma-1} - \frac{\rho E}{p}, \frac{\rho\boldsymbol{v}}{p}, -\frac{\rho}{p}\right],$$

where entropy is $s = \log\left(\frac{p}{\rho^\gamma}\right)$ (see [30] for more details).

The Navier-Stokes equations in entropy form, as represented by Eqn. (2), are then discretized using a space-time discontinuous Galerkin (DG) finite-element formulation. The spatial domain is partitioned using non-overlapping hexahedral elements (κ), and the time domain is partitioned into time intervals ($I^n = [t^n, t^{n+1}]$). Assuming piecewise polynomial functions in both space and time, Eqn. (2) can be written in weak form as:

$$\sum_\kappa \left\{ \int_I \int_\kappa -\left(\boldsymbol{w}_{,t}\boldsymbol{q} + \boldsymbol{w}_{,i}(\boldsymbol{F}_i^I + \boldsymbol{F}_i^V)\right) + \int_I \int_{\partial\kappa} \boldsymbol{w}(\widehat{\boldsymbol{F}_i^I n_\iota} + \widehat{\boldsymbol{F}_i^V n_\iota}) + \int_\kappa \left(\boldsymbol{w}(t_-^{n+1})\boldsymbol{q}(t_-^{n+1}) - \boldsymbol{w}(t_+^n)\boldsymbol{q}(t_+^n)\right) \right\} = 0 \tag{3}$$

where, $\boldsymbol{w}$ is the Lagrange basis function defined at Gauss-Legendre points. The inviscid numerical fluxes, $\widehat{\boldsymbol{F}_i^I n_\iota}$, and viscous numerical fluxes, $\widehat{\boldsymbol{F}_i^V n_\iota}$, across the jump are calculated using Ismail and Roe's flux [31] and the Bassi and Rebay diffusion operator [32], respectively. Integrals in Eqn. (3) are approximated with a quadrature rule using twice the number of quadrature points as solution points in each coordinate direction in order to minimize quadrature errors. The resulting nonlinear system of equations is then solved using a preconditioned Jacobian-free Newton-Krylov solver. Further details regarding the numerical method can be found in Refs. [26] and [27].

The improved efficiency of this high-order scheme for turbulent flows was demonstrated in [27]. Figure 1, reproduced from [27], shows the error in the kinetic energy balance for the Taylor-Green vortex evolution. The 8th-order scheme provides order-of-magnitude reductions in computational cost to achieve the same error tolerance over the lower-order schemes. The goal of the present effort is to bring these efficiencies to turbomachinery simulations.
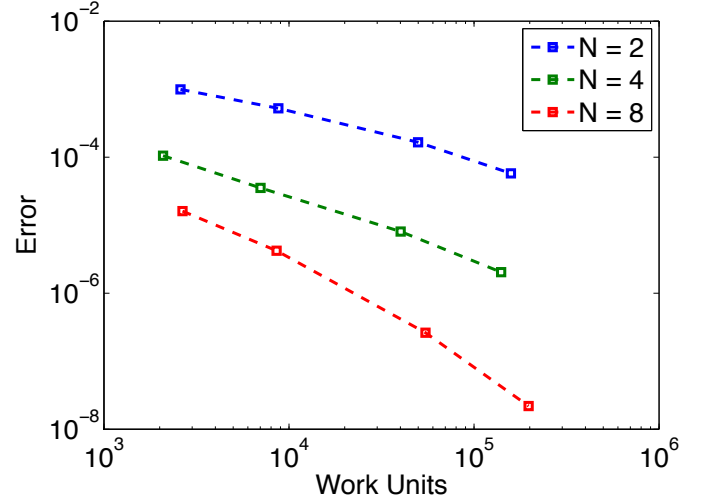

Figure 1. Error in kinetic energy balance as a function of normalized CPU time for Taylor-Green vortex simulation using the present method [27].

EXPERIMENTAL SETUP AND FLOW CONDITIONS

The T106A-EIZ low-pressure turbine cascade configuration experimentally studied by Stadtmuller [29] is considered in the present study. The airfoil profile represents the mid-span section of the Pratt and Whitney PW2037 rotor blade. The experiments were performed with very low freestream turbulence, and both with and without cylindrical bars moving upstream of the airfoil cascade to simulate the wakes generated from an upstream airfoil row. At the exit to the cascade, the isentropic Reynolds number was relatively low, about 60,000, and the Mach number was 0.405. The T106A airfoil profile has also been investigated experimentally in a linear cascade by Stieger et al. [33-34] at different Reynolds numbers. For the present code validation study, we have selected the T106A-EIZ dataset with "clean" inflow conditions where the upstream moving bars are removed and the inflow turbulence is low enough to be neglected. This test case has been used extensively in the literature for code validation studies (see, for example, Refs. [1-5], [10-13]). The operating conditions for the selected test case are shown in Table 1, and geometrical details of the experimental configuration are shown in Fig. 2. As noted in Ref. [11], there is some uncertainty regarding the actual inlet conditions used in the experiments. We have chosen the inlet flow angle, β_1, as 45.5° in order to be consistent with other simulations in the literature (see, for example, Refs. [3, 10, 11]).

3   Copyright © 2015 by ASME

Exit Reynolds number, Re_{2is}	60000
Exit Mach number, Ma_{2is}	0.405
Inflow Mach number, Ma_1	0.286
Pressure ratio, p_2/p_{t1}	0.895

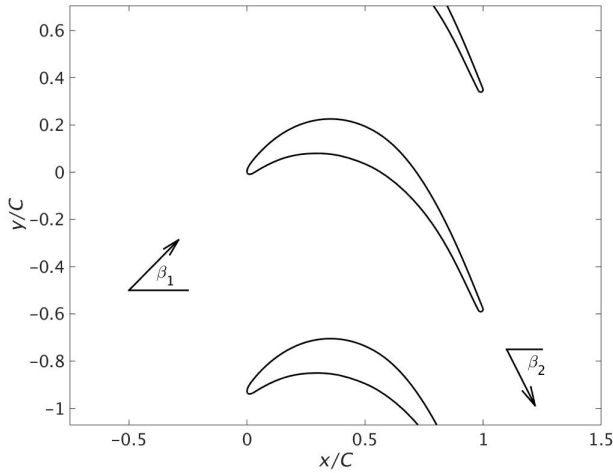Table 1. Operating conditions for the selected T106A-EIZ test case.

Figure 2. Geometrical details of the T106A-EIZ cascade.

COMPUTATIONAL DETAILS

In order to handle the complex geometry of turbomachinery configurations at arbitrarily high order accuracy, the spectral isoparametric mapping demonstrated in Ref. [27] is extended to multiblock configurations. Figure 3 shows a two-dimensional spanwise section of the cascade passage and illustrates the multiblock approach used to discretize the domain. Each individual block uses a separate isoparametric mapping, and the faces between each block are treated as DG element interfaces. In this manner, any combination of number of elements and element order can be used within each grid block.

In the region adjacent to the blade, an O-grid topology is used up to about twice the boundary-layer thickness (at the 0.9930C location, where C is the axial chord length) in the wall-normal direction, and an H-grid topology is used on the rest of the blade passage. The airfoil O-grid is then partitioned into 6 different blocks to match the neighboring H-blocks. The 2D grid is extruded in the spanwise direction to generate the 3D grid. The spanwise extent of the computational domain is chosen as 20% of the chord length. This spanwise extent was deemed to be sufficient for capturing the largest turbulent scales based on other DNS simulations of LPT cascades with similar geometries but different airfoil pitch reported in the literature [1, 5].

Spectral elements are generated for each grid from this multiblock grid. For the blocks adjacent to the airfoil, three

elements are used in the direction normal to the airfoil surface; the height of the first element near the wall is 0.007C and the elements are uniformly stretched in the wall-normal direction. This results in the wall-normal extent of the first element near the wall being roughly 20 and 5 wall units in the fore ($x <$ 0.6C), and aft regions ($x > 0.6C$) of the airfoil suction surface, respectively, and about 8 wall units on the pressure surface. Along the blade surface (tangential direction), the element size is varied from 0.0046C to 0.046C on the suction side, and from 0.03C to 0.26C on the pressure side, with the elements being clustered in the leading and trailing edge regions. Coarser elements are used on the pressure side than on the suction side since the experiments show that the pressure side flow is laminar. To resolve the trailing edge wake, elements of size about 0.02C in the streamwise direction and 0.06C in the transverse direction are used. The inflow and outflow boundaries are located about 2C and C, respectively, from the leading and trailing edge. Eight elements are used in the spanwise direction, resulting in the spanwise extent of a single element being 0.029C. This results in a total of 7408 elements in the airfoil passage. The nodal locations for a single airfoil passage using 2nd-, 4th-,and 8th-order elements are shown in Fig. 4. The total number of degrees of freedom using 2nd-, 4th-, and 8th-order elements are 0.06M, 0.47M, and 3.8M, respectively.
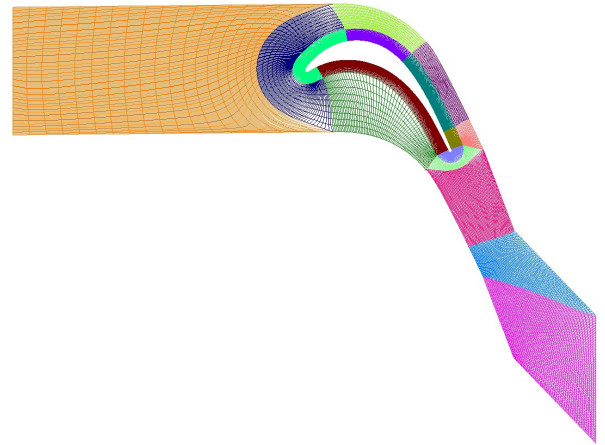

Figure 3. Discretized blade passage using multiblock approach. The different colors in the figure represent different blocks.
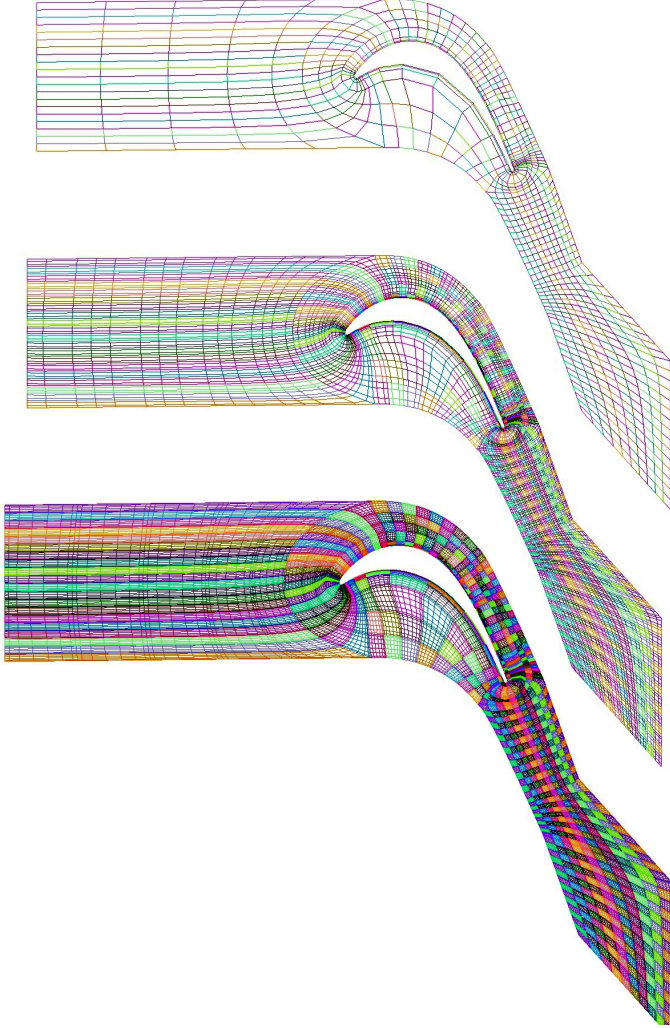
Figure 4. Computational mesh used to represent a spanwise section of the airfoil passage. The top, middle, and bottom figures denote 2nd-, 4th-, and 8th-order elements, and different colors are used to represent individual elements.

RESULTS

In the current simulations, elements that are 2nd-, 4th-, and 8th-order in space and 4th-order in time are used with a convective CFL number of 5. The simulations are carried out for a total of 28 flow-through times, where the flow-through time is defined by $C/Ma_1 a_1$. Flow statistics are then calculated by averaging over the last twenty flow-through times.

Periodic boundary conditions are used in the pitchwise and spanwise direction. On the airfoil surface, a no-slip adiabatic wall boundary condition is used. At the subsonic inflow boundary, four quantities, total pressure, two flow angles, and a Riemann invariant are specified. A second Riemann invariant is extrapolated from the interior of the domain at the inlet boundary to complete the system of equations needed to uniquely prescribe the inlet conditions. At the subsonic outflow boundary, an approximate 1-D Riemann problem is solved with

the exit static pressure specified, and the remaining variables being extrapolated from the interior.

Figure 5a compares the airfoil loadings ($C_p = \frac{p - p_2}{p_{t,1} - p_2}$) from the simulations at different spatial orders with the experimental data. For DG schemes, the numerical solutions are discontinuous at the element boundaries. When the resolution is inadequate, this is reflected in a saw-tooth profile as in the results from the 2nd-order simulation in the figure. With the increase of element spatial order, the resolution of the computed flow-field improves and the numerical solution is smooth and converges to the experimental data. The 4th-order and 8th-order results are almost identical to each other except in the local vicinity of the trailing edge separation region on the suction surface.

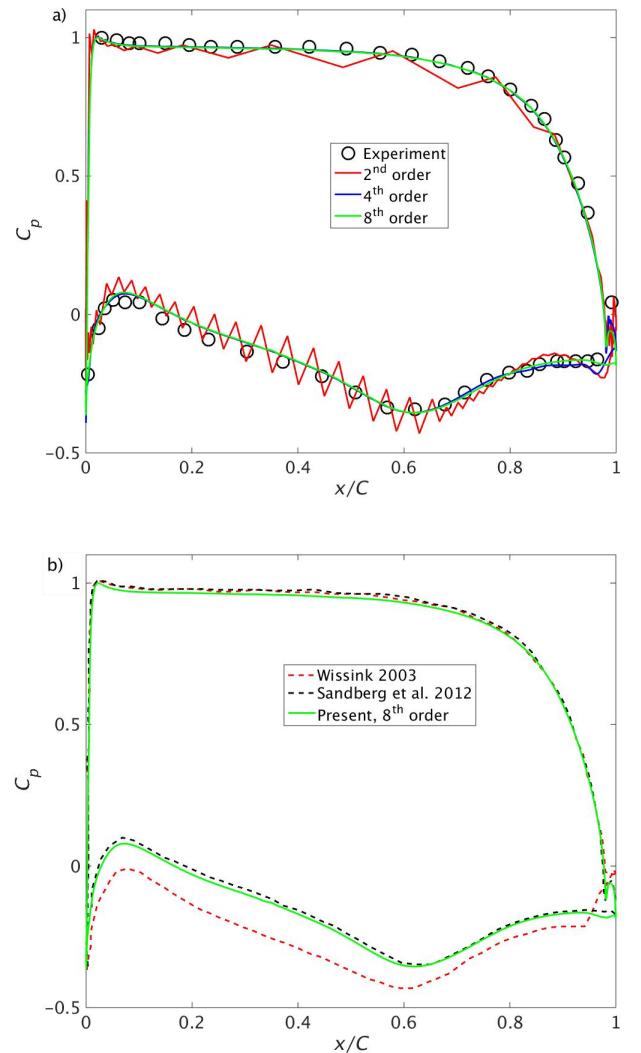Figure 5. Comparison of airfoil loadings between (a) present simulations with different solution order and experiment; and (b) present 8th order simulations and other published compressible and incompressible DNS results.

Figure 5b compares the airfoil loadings with DNS results published in the literature for the same configuration. The DNS results of Wissink [3] were obtained using a second-order accurate finite-volume incompressible flow solver with about 25M grid points. Since compressibility effects are ignored, the results of Ref. [3] predict much stronger peak suction. More recently, Sandberg et al. [10] have presented DNS results for the same configuration using a compact 4th-order finite-difference scheme in a compressible formulation using around 18M grid points. As shown in the figure, the 8th-order simulation results from the present study are in good agreement with the results of Ref. [10] and the experimental data. The present 8th-order simulation achieves similar accuracy as the 4th-order results of Ref. [10] using much fewer degrees of freedom.

Figure 6 compares the wall shear stress coefficient $(C_f = \frac{\tau_w}{p_{t1} - p_2})$ obtained from the present simulations with different solution order. As with the airfoil loadings in Fig. 5, Fig. 6 shows that the shear stress coefficient for the 4th-order and 8th-order solutions are very close to each other on the pressure side of the airfoil and on the suction side except in the vicinity of the trailing edge. The wall shear stress coefficient for the 2nd-order solution, on the other hand, is much higher. The oscillations in the 8th-order results on the suction surface of the airfoil in the region $0.25C < x < 0.4C$ can be traced to the use of a low-order geometry representation for the airfoil in the simulations. These oscillations become more prominent with increasing solution order in regions of high curvature and highlight the importance of using higher-order geometry approximations in conjunction with high-order simulations. This issue is being addressed in future simulations.
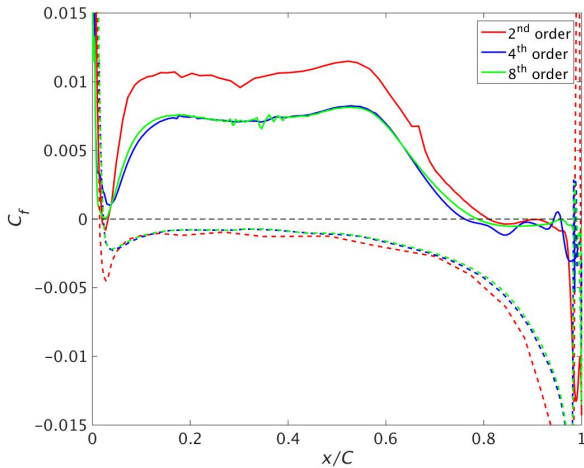

Figure 6. Comparison of wall shear stress coefficient obtained with different solution orders. The solid and dashed line represent the airfoil suction and pressure surfaces, respectively. The thin dashed black line denotes the $C_f = 0$ location.

The wake deficits computed in the present study are presented and compared to experiments and other numerical simulations in Fig. 7 at a location $0.4C$ downstream of the trailing edge of the airfoil. The wake deficit is evaluated as the total pressure loss coefficient:

$$\omega_u = \frac{p_{t1} - p_t}{p_{t1} - p_2}. \qquad (4)$$

and is plotted from the suction side to the pressure side in Fig. 7. As noted in the literature, the wake deficit in such low Reynolds number flows is difficult to accurately capture in RANS simulations incorporating transition models. These RANS simulations generally underestimate the wake width and overestimate the pressure loss [25]. Figure 7 shows that the estimated wake deficit for the 8th-order solution compares well with the experiment. Note that, following Ref. [10], the experimental data in Fig. 7 has been shifted in the pitchwise direction since the exact measurement position is not known. Although the 4th-order solution matched well with the 8th-order solution for the airfoil loadings, differences between the two solutions can be seen in the wake deficit. As would be expected, the 2nd-order solution fails to predict the wake losses. The results of Ref. [10] are also plotted on the figure for comparison and are similar to the present results obtained with much fewer degrees of freedom. The exit flow angle of 63° obtained from the present simulations compares well with the experimental value of 63.5°.
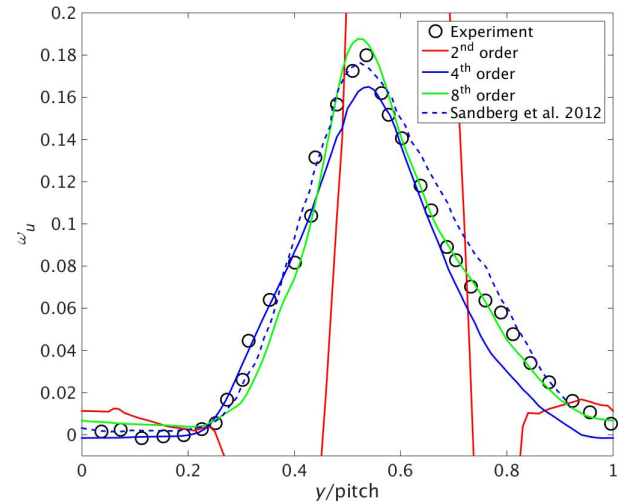

Figure 7. Comparison of wake loss profiles obtained in the present study with experimental and other numerical results.

The computed velocity field from the 8th-order solution is examined in more detail in Figs. 8-10. Figure 8 presents the instantaneous velocity magnitude in the turbine cascade across the mid-span section of the domain. The flow remains attached and laminar on the pressure side, and the stagnation point is located at $x \approx 0.05C$. On the suction surface, the flow accelerates in the region $0 < x < 0.5C$ and the boundary layer remains attached. As the flow decelerates along the aft portion of the suction surface of the airfoil, a separation bubble forms beyond the streamwise location $x > 0.7C$. Downstream of the separation bubble, the flow becomes turbulent.
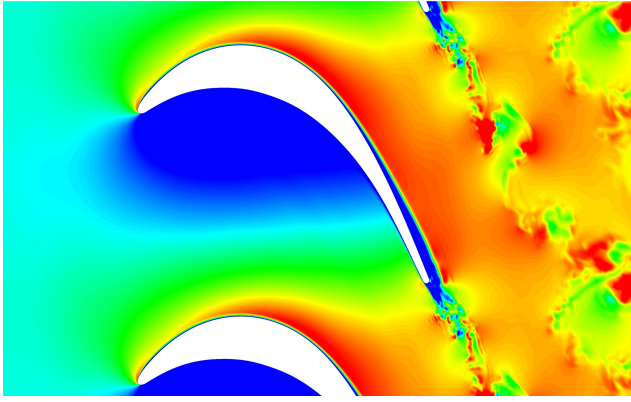
Figure 8. Instantaneous velocity magnitude profile across the mid-span section of the computational domain. Additional airfoils are periodically replicated for clarity.

Figure 9. Mean velocity magnitude profile (top) and turbulent intensity (bottom) with respect to the tangential and wall-normal direction.
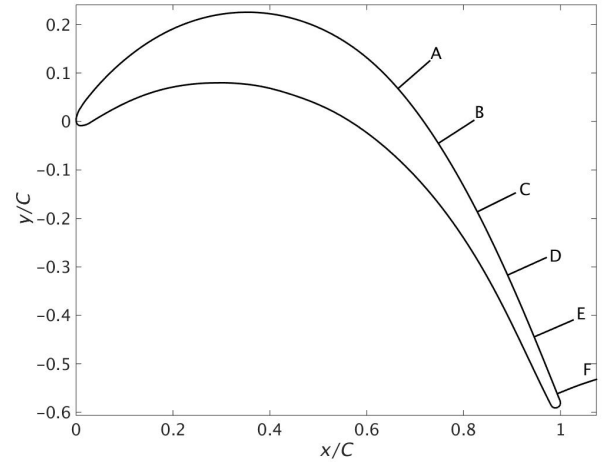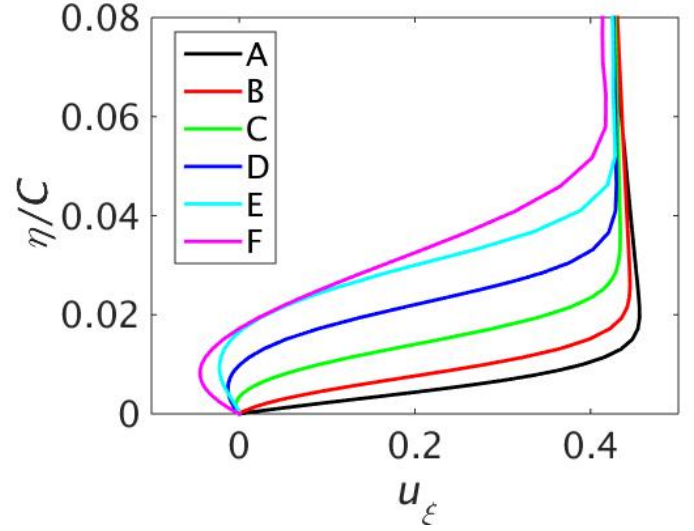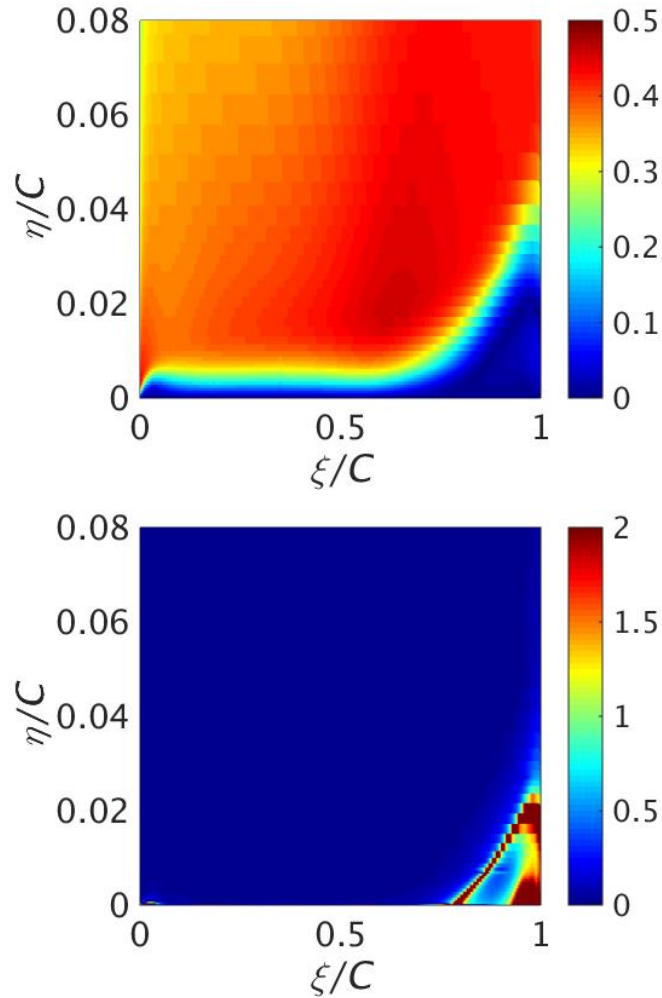

Figure 10. Streamwise velocity profiles at various locations on the airfoil suction surface corresponding to (A) $\xi = 0.6645C$, (B) $\xi = 0.7478C$, (C) $\xi = 0.8284C$, (D) $\xi = 0.8909C$, (E) $\xi = 0.9457C$, and (F) $\xi = 0.9933C$. The locations along the airfoil surface corresponding to the velocity profile stations are shown in the bottom figure for reference.

Fig. 9 shows color contour plots of the mean velocity magnitude (U) and turbulence intensity (Tu = $\frac{1/3\sqrt{u^2+v^2+w^2}}{U}$) with respect to the tangential (ξ) and wall-normal (η) directions on the airfoil suction surface. As the flow accelerates in the fore region, the boundary-layer remains laminar and its thickness changes marginally. In the aft region, a separation bubble forms as the flow decelerates and the boundary-layer thickness increases rapidly. Flow separation results in a strong shear, which in turn increases the turbulence intensity in the aft region of the suction surface as shown in Fig. 9.

Streamwise velocity (u_ξ) profiles at various locations on the suction surface in the aft region of the airfoil are plotted in

Fig. 10. The velocity profiles show the flow separation on the suction surface between the locations B and C marked on the figure.

Figure 11 shows the instantaneous spanwise vorticity contours along the midspan location of the turbine cascade. The separation bubble near the suction surface trailing edge moves the shear layer away from the suction surface and the flow transitions to turbulence. Laminar vortex shedding from the pressure surface shear layer undergoes laminar rollup, whereas on the suction side the rollup is less evident due to turbulence. Downstream of the airfoil trailing edge, the laminar and turbulent shear layers merge to form a fully turbulent wake Although the 8th-order solution compares well with the experimental pressure loadings and wake loss data, small discontinuities in the spanwise vorticity contours can be noticed in Fig. 11. The breakdown to turbulence of the flow in the aft region of the suction surface can be seen in the isosurfaces of spanwise vorticity in Fig. 12.
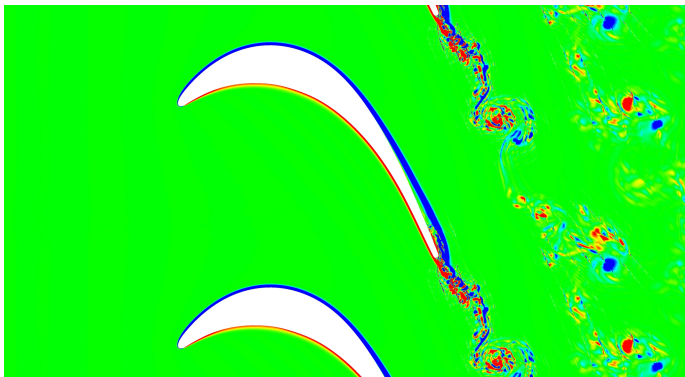

Figure 11. Instantaneous spanwise vorticity contours in the midspan of the computational domain. Additional airfoils are periodically replicated for clarity.
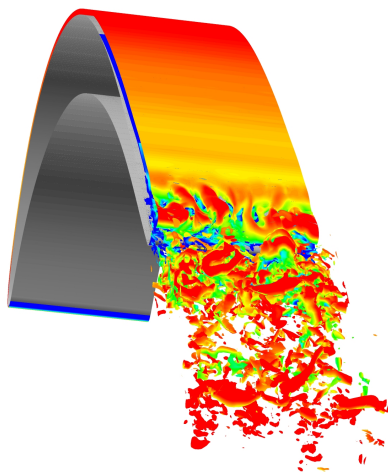

Figure 12. Three-dimensional view of the aft region of the suction surface of the airfoil showing isosurfaces of instantaneous spanwise vorticity.

CONCLUDING REMARKS

Results from a DNS of transitional and turbulent flow in a linear turbine cascade using a high-order entropy-stable DG spectral-element method with a space-time formulation are described. The predicted airfoil pressure loadings using 8th-order accurate spatial and 4th-order accurate temporal discretizations agree well with the experimental data. For this lightly loaded, low Reynolds number turbine cascade, the flow remains laminar on the pressure surface, but undergoes transition on the suction surface. In the fore region of the airfoil suction surface the boundary-layer remains attached and laminar, but in the aft region the boundary layer separates due to the decelerating flow. A separation bubble is noted on the suction surface at about the $0.7C$ streamwise location. The separation bubble produces strong shear and generates turbulence downstream. These flow features are reflected in the wake loss profile that shows the wake loss increases more rapidly on the suction side compared to the pressure side.

The results presented here represent a first validation of the applicability of the DG spectral-element methodology for turbomachinery flow computations.

REFERENCES

1. Wu, X., and Durbin, P. A., "Evidence of Longitudinal Vortices Evolved from Distorted Wakes in a Turbine Passage," *Journal of Fluid Mechanics*, 446, pp. 199-228, 2001.

2. Kalitzin, G., Wu, X., and Durbin, P. A., "DNS of Fully Turbulent Flow in a LPT Passage," *International Journal of Heat and Fluid Flow*, 24, pp. 636-644, 2003.

3. Wissink, J. G., "DNS of Separating, Low Reynolds Number Flow in a Turbine Cascade with Incoming Wakes," *International Journal of Heat and Fluid Flow*, 24, pp. 626-635, 2003.

4. Wissink, J. G., and Rodi, W., "Direct Numerical Simulation of Flow and Heat Transfer in a Turbine Cascade with Incoming Wakes," *Journal of Fluid Mechanics*, 569, pp. 209-247, 2006.

5. Zaki, T. A., Wissink, J. G., Rodi, W., and Durbin, P. A., "Direct Numerical Simulation of Transition in a Compressor Cascade: The Influence of Free-Stream Turbulence," *Journal of Fluid Mechanics*, 665, pp. 57-98, 2010.

6. Rai, M. M., "A Direct Numerical Simulation of Transitional and Turbulent Flow on a Turbine Airfoil," AIAA Paper 2006-4460, July 2006.

7. Rai, M. M., "A Direct Numerical Simulation of Transition and Turbulence in a Turbine Stage," AIAA Paper 2009-584, Jan. 2009.

8. Rai, M. M., "A Direct Numerical Simulation of Stator-Rotor Interaction in an Axial Compressor," AIAA Paper 2010-6533, July 2010.

9. Rai, M. M., "A Direct Numerical Simulation of Flow Through a Low Pressure Turbine Stage," AIAA Paper 2011-3092, June 2011.

10. Sandberg, R. D., Pichler, R., and Chen, L., "Assessing the Sensitivity of Turbine Cascade Flow to Inflow Disturbances Using Direct Numerical Simulation," Proceedings of 13th International Symposium for Unsteady Aerodynamics, Aeroacoustics and Aeroelsticity in Turbomachinery, Tokyo, Japan, 2012.

11. Sandberg, R. D., Pichler, R., Chen, L., Johnstone, R., and Michelassi, V., "Compressible Direct Numerical Simulation of Low-Pressure Turbines: Part I – Methodology," Proceedings of ASME Turbo Expo, Paper GT2014-2568, Dusseldorf, Germany, 2014.

12. Michelassi, V., Chen, L. W., Pichler, R., and Sandberg, R. D., "Compressible Direct Numerical Simulation of Low-Pressure Turbines: Part II – Effect of Inflow Disturbances," Proceedings of ASME Turbo Expo, Paper GT2014-25689, Dusseldorf, Germany, 2014.

13. Michelassi, V., Wissink, J. G., Frohlich, J., and Rodi, W., "Large-Eddy Simulation of Flow Around Low-Pressure Turbine Blade with Incoming Wake," *AIAA Journal*, 41, pp. 2143-2156, 2003.

14. Raverdy, B., Mary, I., Sagaut, P., and Liamis, N., "High-Resolution Large-Eddy Simulation of Flow Around Low-Pressure Turbine Blade," *AIAA Journal*, 41, pp. 390-397, 2003.

15. Matsuura, K., and Kato, C., "Large Eddy Simulation of Compressible Transitional Flows in a Low-Pressure Turbine Cascade," *AIAA Journal*, 45, pp. 442-457, 2007.

16. Sarkar, S., and Voke, P. R., "Large-Eddy Simulation of Unsteady Surface Pressure over a Low-Pressure Turbine Blade Due to Interaction of Passing Wakes and Inflexional Boundary Layer," *Journal of Turbomachinery*, 128, pp. 221-231, 2006.

17. Medic, G., and Sharma, O., "Large-Eddy Simulation of Flow in a Low-Pressure Turbine Cascade," Proceedings of ASME Turbo Expo, Paper GT2012-68878, Copenhagen, Denmark, 2012.

18. You, D., Wang, M., Moin, P., and Mittal, R., "Large-Eddy Simulation Analysis of Mechanisms for Viscous Losses in a Turbomachinery Tip-Clearance Flow," *Journal of Fluid Mechanics*, 586, pp. 177-204, 2007.

19. Mishra, A., and Bodony, D. J., "Evaluation of Actuator Disk Theory for Predicting Indirect Combustion Noise," *Journal of Sound and Vibration*, 332, pp. 21-38, 2013.

20. Bassi, F., Crivellini, A., Rebay, S., Savini, M., "Discontinuous Galerkin solution of the Reynolds-Averaged Navier–Stokes and k–x Turbulence Model Equations," *Computers and Fluids*, 34. pp. 507–540, 2005.

21. Corsini, A., Rispoli, F., Santoriello, A., "A Variational Multiscale Higher-Order Finite-Element Formulation for Turbomachinery Flow Computations," *Computer Methods in Applied Mechanics and Engineering*, 194, pp. 4797–4823, 2005.

22. Cherednichenko, S., Frey, C., and Ashcroft, G., "On the Application of the Discontinuous Galerkin method to Turbomachinery Flows," European Congress on Computational Methods in Applied Sciences and Engineering (ECCOMAS 2012). J. Eberhardsteiner et.al. (eds.) Vienna, Austria, 2012.

23. Ghidoni, A., Colombo, A., Rebay, S., "Simulation of the Transitional Flow in a Low Pressure Gas Turbine Cascade with a High-Order Discontinuous Galerkin Method," *Journal of Fluids Engineering*, 135, 071101, 2013.

24. De Wiart, C. C., Hillewaert, K., and Geuzaine, P., "DNS of a Low Pressure Turbine Blade Computed with a Discontinuous Galerkin method," Proceedings of ASME Turbo Expo, Paper GT2012-68900, Copenhagen Denmark, 2012.

25. Hillewaert, K., Verheylewegen, G., and Arts, T., "Assessment of a High-Order Discontinuous Galerkin Method for the Direct Numerical Simulation of Transition at Low-Reynolds Number in the T106C High-Lift Low Pressure turbine Cascade," Proceedings of ASME Turbo Expo, Paper GT2014-26739, Dusseldorf, Germany, 2014.

26. Diosady, L. T., and Murman, S. M., "Design of a Variational Multiscale Method for Turbulent Compressible Clows," AIAA Paper 2013-2870, July 2013.

27. Diosady, L. T., and Murman S. M., "DNS of Flows over Periodic Hills Using a Discontinuous-Galerkin Spectral-Element Method," AIAA Paper 2014-2784, July 2013.

28. Murman, S. M., Diosady, L. T., and Garai, A., "Development of Dynamic Sub-Grid Modeling for Variational Multiscale Methods," Proceedings of the Summer Program 2014, Center for Turbulence Research, Stanford University, Stanford, CA, 2014.

29. Stadtmuller, P., "Investigation of Wake-Induced Transition on the LP Turbine Cascade T106A-EIZ," DFG-Verbundprojekt Fo 136//11, Version 1.0, University of the Armed Forces Munich, Germany.

30. Hughes, T. J. R., Franca, L., and Mallet, M., "A New Finite Element Formulation for Computational Fluid Dynamics: I Symmetric Forms of the Compressible Euler and Navier-Stokes equation and the Second Law of Thermodynamics," *Computer Methods in Applied Mathematics*, 54, pp. 223-234, 1986.

31. Ismail, F., and Roe, P. L., "Affordable, Entropy-Consistent Euler flux Functions II: Entropy Production at Shocks," *Journal of Computational Physics*, 228, pp. 5410-5436, 2009.

32. Bassi, F., and Rebay, S., "GMRES Discontinuous Galerkin Solution of the Compressible Navier-Stokes Equations," Discontinuous Galerkin Methods: Theory, Computation and Applications, edited by K. Cockburn and Shu, Springer, Berlin, pp. 197-208, 2000.

33. Stieger, R. D., Hollis, D., and Hodson, H. P., "Unsteady Surface Pressures due to Wake Induced Transition in a Laminar Separation Bubble on a LP Turbine Cascade," Proceedings of ASME Turbo Expo, Paper GT2003-38303, Atlanta, USA, 2003.

34. Stieger, R. D., and Hodson, H. P., "The Transition Mechanism of Highly-Loaded LP Turbine Blades," Proceedings of ASME Turbo Expo, Paper GT2003-38304, Atlanta, USA, 2003.